In silico analysis of metabolic burden effects on a multicellular integral controller

Giovanni Campanile, Vittoria Martinelli, Davide Salzano, Davide Fiore and Mario di Bernardo

***Abstract*— Metabolic burden is a critical limiting factor in the design of synthetic circuits, affecting both their reliability and performance. To mitigate its effects, distributing control functions across different cell populations within a multicellular control architecture offers a promising solution, while simultaneously enhancing modularity and re-usability of the circuits. We first present a model that explicitly accounts for limited ribosome availability within cells. Using this framework, we then derive a mathematical model of a multicellular antithetic integral controller that incorporates these shared resources. Through numerical bifurcation analysis and *in silico* agent-based experiments in BSim, we compare the multicellular controller against its traditional single-cell (embedded) implementation, evaluating both resource utilization and stability.**

I. Introduction

Synthetic biology aims to create novel functionalities in living organisms through engineered genetic networks. Applications span diverse fields including medicine, agriculture, energy, and environmental protection. Engineered bacteria, for instance, can detect and target cancer cells [1], [2], produce bio-fuels [3], or remediate harmful substances from water and soil [4]. However, the inherent nonlinearity, stochasticity, and variability of biological systems can limit their practical applications. Control theory offers powerful tools to address these limitations, enhancing the stability, robustness, and performance of synthetic biological systems. This interface between control and biology has given rise to *Cybergenetics*, which focuses on developing biochemical controllers for engineering reliable and robust synthetic cells. A crucial element in this field is the implementation of an integral action, which enables synthetic circuits to achieve and maintain desired outputs despite disturbances—a property known as *robust perfect adaptation (RPA)* [5].

The first Antithetic Integral Controller (AIC), introduced in [5], utilizes a pair of proteins that bind with high affinity to form an inert complex. These proteins are produced in proportion to the reference signal and the output gene requiring regulation. While both numerical and experimental studies have demonstrated this controller's ability to achieve RPA [5], [6], implementing all control components within single cells can compromise stability and performance. A primary constraint is metabolic burden, that is, the competition between engineered networks and native cellular processes for limited resources [7]. This burden can impair cellular physiology, leading to reduced growth and increased mutation rates [8], [9], while also introducing unexpected non-regulatory interactions among chemical species [10]. Patel et al. [11] developed a model that accounts for limited ribosome availability in gene networks. When applied to the antithetic integral controller, their analysis revealed how metabolic burden and its induced non-regulatory interactions can destabilize the circuit.

A promising approach to mitigate metabolic burden is the distribution of control functions across different populations within a microbial consortium, implementing a multicellular control architecture [12]–[14]. It has been claimed that this strategy can enhance modularity and re-usability of engineered cells while enabling separation of incompatible chemical reactions and reducing the metabolic load on individual populations. Consequently, microbial consortia can achieve improved production throughput and survivability.

This paper presents an *in silico* investigation of metabolic burden effects on both embedded and multicellular implementations of the AIC. We first derive a model that explicitly incorporates intracellular resource competition in the embedded controller. We then develop a multicellular implementation comprising two microbial populations that communicate via orthogonal quorum sensing molecules. After deriving a resource-aware model of the consortium, we analyze equilibrium stability through numerical bifurcation analysis. The multicellular design is validated using *BSim*, a realistic agent-based simulator [15], with *in silico* experiments. Finally, we compare both architectures in terms of regulation capability and resource utilization efficiency.

II. Background

This section reviews key concepts of the antithetic integral controller in two configurations: an *embedded* version, where both integral control and target processes reside within a single cell, and a *multicellular* version, where these processes are distributed across two distinct cell populations. We also present the mathematical framework used to model the effects of limited ribosome availability. Throughout this paper, we use capital letters (e.g., X) to denote genes and proteins, and lowercase letters (e.g., x) to represent their concentrations.

Giovanni Campanile, Vittoria Martinelli and Davide Fiore are with the Department of Mathematics and Applications "R. Caccioppoli," University of Naples Federico II, 80126 Naples, Italy (e-mail: giov.campanile@studenti.unina.it, vittoria.martinelli@unina.it, davide.fiore@unina.it). Davide Salzano is with the Department of Electrical Engineering and Information Technology, University of Naples Federico II, 80125 Naples, Italy (e-mail: davide.salzano@unina.it).Mario di Bernardo is with the Department of Electrical Engineering and Information Technology, University of Naples Federico II, 80125 Naples, Italy, and also with the SSM School for Advanced Studies, 80138 Naples, Italy (e-mail: mario.dibernardo@unina.it). This work has received financial support by the European Union - Next Generation EU, under PRIN 2022 PNRR, Project "Control of smart microbial communities for wastewater treatment".

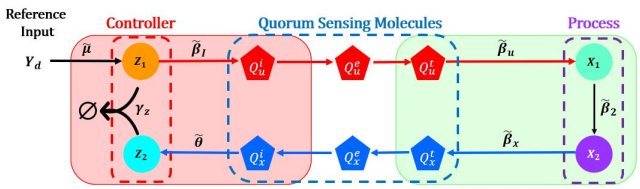

Fig. 1: Architecture of the multicellular AIC. The genetic circuit is distributed across two microbial populations: the Controllers (in red) host species Z_1 and Z_2, the Targets (in green) host species X_1 and X_2. Orthogonal quorum sensing molecules Q_u and Q_x, the red and blue polygons, respectively, implement the communication protocol by diffusing into the environment.

A. Embedded AIC

Robust perfect adaptation (RPA)—the ability to maintain stable, predictable behavior across varying environmental conditions and cellular states—is essential for engineered biological systems. The antithetic motif [5], a synthetic gene network capable of integral control action, has been demonstrated to achieve RPA. This controller employs two high-affinity sequestering biomolecular species, Z_1 and Z_2, to regulate a biological process involving genes X_1 and X_2, where X_2 production depends on X_1. The feedback loop is completed by Z_1 promoting X_1 production and Z_2 being produced proportionally to X_2. Under the assumption of unlimited cellular resources, the system dynamics can be described as [16]

$$\begin{aligned} \dot{x}_1 &= \beta_I z_1 - \gamma x_1, \\ \dot{x}_2 &= \beta_2 x_1 - \gamma x_2, \\ \dot{z}_1 &= \mu Y_d - \gamma_z z_1 z_2, \\ \dot{z}_2 &= \theta x_2 - \gamma_z z_1 z_2. \end{aligned} \tag{1}$$

In this model, β_I, β_2, μ and θ represent the activation rates of X_1, X_2, Z_1 and Z_2 respectively, with β_I serving as the integral control gain. The dilution rate of X_1 and X_2 is denoted by γ, while γ_z represents the binding rate between Z_1 and Z_2, assumed to be their sole degradation mechanism, following [16]. The reference signal Y_d is either provided externally or encoded constitutively in the Z_1 promoter. The difference $(z_1 - z_2)$ is proportional to the integral of the control error $e(t) := \mu Y_d - \theta x_2$, thus implementing integral control [5].

B. Multicellular AIC

A multicellular implementation of the AIC can be derived from the multicellular PI control architecture in [13] by removing the proportional controller cells. This design separates the integral control action and the biological process into two distinct populations: a *Controller* population and a *Target* population (see Fig. 1). Communication between populations occurs via two orthogonal quorum sensing molecules: Q_u, which delivers the control input to target cells as an actuation signal, and Q_x, which acts as a sensing signal, effectively closing the feedback loop.

Throughout the rest of the paper, superscripts e, t, and c denote quantities in the environment, Target cells, and Controller cells, respectively.

The Target cells contain the same controlled process described in Section II-A, comprising genes X_1 and X_2. The molecule Q_u activates X_1, while Q_x (the measured output) is produced in proportion to X_2. Assuming the diffusion dynamics of the quorum sensing molecules to be linear [17], the dynamics of the species within the target cells can be described by

$$\dot{x}_1 = \beta_u q_u^t - \gamma_t x_1, \tag{2}$$
$$\dot{x}_2 = \beta_2 x_1 - \gamma_t x_2, \tag{3}$$
$$\dot{q}_x^t = \beta_x x_2 + \eta (q_x^e - q_x^t) - \gamma_t q_x^t, \tag{4}$$

where β_u and β_x are the activation rates of X_1 and Q_x, respectively, and γ_t is the dilution rate of the target cells. Additionally, η is the diffusion rate of the molecules across the cell membrane, assumed to be the same for all cells [18].

The quorum sensing molecule Q_u is produced by the controller cells embedding the antithetic motif described in Section II-A. The dynamics of the network hosted within the controller cells can thus be written as

$$\dot{z}_1 = \mu Y_d - \gamma_z z_1 z_2, \tag{5}$$
$$\dot{z}_2 = \theta q_x^c - \gamma_z z_1 z_2, \tag{6}$$
$$\dot{q}_u^c = \beta_I z_1 + \eta (q_u^e - q_u^c) - \gamma_c q_u^c, \tag{7}$$

where β_I is the activation rate of Q_u playing the role of the integral gain, and γ_c is the dilution rate of the quorum sensing molecules inside the controller cells.

The dynamics of Q_u and Q_x in the population not producing them can be described by

$$\begin{aligned} \dot{q}_u^t &= \eta (q_u^e - q_u^t) - \gamma_t q_u^t, \\ \dot{q}_x^c &= \eta (q_x^e - q_x^c) - \gamma_c q_x^c. \end{aligned} \tag{8}$$

Finally, the dynamics of the quorum sensing molecules in the environment is given by

$$\dot{q}_k^e = \eta \sum_{j \in \mathscr{S}} N_j (q_k^j - q_k^e) - \gamma_e q_k^e, \tag{9}$$

where $k \in \{x, u\}$, $\mathscr{S} = \{t, c\}$ and N_j is the number of cells in each population. All the other parameters of the consortium have the same meaning as in (1). Note that in the model described in this section, it is assumed to have unlimited cellular resources.

C. Burden model

Gene expression depends on finite cellular resources, including chemical species, RNA polymerase, and ribosomes [10]. In this work, we focus on the limited availability of free ribosomes – which translate mRNA into amino acid chains to form proteins – as the primary constraint on gene expression. This choice is supported by experimental evidence identifying ribosomes as a key limiting factor in bacterial gene expression during exponential growth [10], [19].

Since ribosomes are finite in number and can only translate one mRNA at a time, their availability directly affects protein

production rates throughout the cell. To capture these cross-coupling effects, we employ the *burden* model introduced in [11], which we briefly summarize here for completeness.

Consider the following set of chemical reactions describing the process of synthesis of protein X_p

$$\begin{gathered}\emptyset \xrightarrow{u\cdot\alpha_m} X_m \xrightarrow{\gamma_m} \emptyset \\ X_m + R \underset{\mathsf{k}^-}{\overset{\mathsf{k}^+}{\rightleftharpoons}} C \xrightarrow{\tilde{\alpha}_p} X_p + R + X_m \\ X_p \xrightarrow{\gamma_p} \emptyset\end{gathered} \tag{10}$$

The first reaction is the transcription of the mRNA X_m of the gene X, that occurs at rate α_m and depends on the presence of the input signal u (e.g. it is constitutively expressed by the promoter or promoted/inhibited by a transcription factor). The mRNA also degrades at rate γ_m. The second reaction represents the binding of the mRNA X_m with a free ribosome R, forming the translation complex C. This reversible reaction happens with forward and reverse rates k^+ and k^-, respectively. Finally, the protein X_p is produced at rate $\tilde{\alpha}_p$ and degrades at rate γ_p.

By applying the law of mass action, the dynamics of X_m, C and X can be described by

$$\begin{aligned}\dot{x}_m &= \alpha_m u - \gamma_m x_m - k^+ R x_m + \tilde{\alpha}_p c + k^- c, \\ \dot{c} &= k^+ x_m R - \tilde{\alpha}_p c - k^- c, \\ \dot{x}_p &= \tilde{\alpha}_p c - \gamma_p x_p.\end{aligned} \tag{11}$$

Since the dynamics of the translation complex C occur much faster than protein dynamics [20], we can apply a quasi-steady state assumption ($\dot{c} \approx 0$), yielding

$$c = \frac{k^+}{k^- + \tilde{\alpha}_p} x_m R = \rho_X x_m R, \tag{12}$$

where $\rho_X := \frac{k^+}{k^- + \alpha_p}$ is termed the resource demand coefficient (RDC) associated to protein X [11]. Under this assumption, model (11) becomes

$$\begin{aligned}\dot{x}_m &= \alpha_m u - \gamma_m x_m, \\ \dot{x}_p &= \tilde{\alpha}_p \rho_X x_m R - \gamma_p x_p.\end{aligned} \tag{13}$$

At each time instant a ribosome can be either free or forming the translation complex of a protein. Denoting as X_i, $i \in \{1, \dots, n\}$ all the synthetic proteins produced within the cell, and assuming the total amount of shared ribosomes to be constant and equal to R_T, we can write

$$\begin{aligned}R_T &= R + \sum_{i=1}^{n} c_i = R + \sum_{i=1}^{n} \rho_i R x_{mi} \\ &= R \left(1 + \sum_{i=1}^{n} \rho_i x_{mi}\right).\end{aligned} \tag{14}$$

This implies that

$$R = \frac{R_T}{1 + \sum_{i=1}^{n} \rho_i x_{mi}}. \tag{15}$$

Finally, assuming also the mRNA dynamics to be at quasi-steady state [20], i.e. $\dot{x}_m \approx 0$, we obtain

$$\dot{x}_p = \tilde{\alpha}_p \rho_X \frac{\alpha_m u}{\gamma_m} \frac{R_T}{1 + \sum_{i=1}^{n} \rho_i x_{mi}} - \gamma_p x_p. \tag{16}$$

III. Effects of metabolic burden on the AIC

This section presents mathematical models with burden for both embedded and multicellular AIC, including their steady-state X_2 values. We first review the embedded AIC model with metabolic burden from [11], then derive a resource-aware model for the multicellular implementation.

A. Embedded AIC with Metabolic Burden

The mathematical model describing the dynamics of the embedded (or single-cell) AIC (1) in the presence of limited resources (i.e. ribosomes) can be obtained by modeling limited ribosomes, as described in equation (16), for all the species implementing the AIC, yielding [11]

$$\begin{aligned}\dot{x}_1 &= \tilde{\beta}_I \rho_{x_1} \frac{\alpha_{x_1}}{\gamma_{x_1}} R z_1 - \gamma x_1, \\ \dot{x}_2 &= \tilde{\beta}_2 \rho_{x_2} \frac{\alpha_{x_2}}{\gamma_{x_2}} R x_1 - \gamma x_2, \\ \dot{z}_1 &= \tilde{\mu} \rho_{z_1} \frac{\alpha_{z_1}}{\gamma_{z_1}} R Y_d - \gamma_z z_1 z_2, \\ \dot{z}_2 &= \tilde{\theta} \rho_{z_2} \frac{\alpha_{z_2}}{\gamma_{z_2}} R x_2 - \gamma_z z_1 z_2,\end{aligned} \tag{17}$$

where α_X / γ_X, with $X \in \{X_1, X_2, Z_1, Z_2\}$ is the ratio between the elongation and the degradation rate of mRNA associated to gene X. $\tilde{\beta}_I$, $\tilde{\beta}_2$, $\tilde{\mu}$ and $\tilde{\theta}$ are the protein synthesis rates of X_1, X_2, Z_1 and Z_2, respectively.

The relationship between these parameters and the corresponding ones in (1) can be directly established in the case of abundant resources (i.e. $R \gg \sum_{i=1}^{n} c_i \implies R \approx R_T$)

$$\begin{aligned}\beta_I &:= \tilde{\beta}_I \rho_{x_1} \frac{\alpha_{x_1}}{\gamma_{x_1}} R_T, \quad \beta_c := \tilde{\beta}_2 \rho_{x_2} \frac{\alpha_{x_2}}{\gamma_{x_2}} R_T, \\ \mu &:= \tilde{\mu} \rho_{z_1} \frac{\alpha_{z_1}}{\gamma_{z_1}} R_T, \quad \theta := \tilde{\theta} \rho_{z_2} \frac{\alpha_{z_2}}{\gamma_{z_2}} R_T.\end{aligned} \tag{18}$$

All the other parameters have the same meaning as in (1) and (16).

The expression of R in (17) can be obtained from (14) by considering the cascade of genes in the AIC, that is

$$R = \frac{R_T}{1 + \rho_{x_1} \frac{\alpha_{x_1}}{\gamma_{x_1}} z_1 + \rho_{x_2} \frac{\alpha_{x_2}}{\gamma_{x_2}} x_1 + \rho_{z_1} \frac{\alpha_{z_1}}{\gamma_{z_1}} Y_d + \rho_{z_2} \frac{\alpha_{z_2}}{\gamma_{z_2}} x_2}. \tag{19}$$

This relationship highlights that the production rate of each protein in (17) depends not only on the concentration of the species that directly activates its expression, but also on the concentration of free ribosomes R in (19), which depends on the concentration of the other proteins in the circuits.

Given some fixed value of the reference signal Y_d and provided that the values of the parameters in (17) are such that the system converges to a stable, admissible equilibrium point (i.e. such that $R \neq 0$), the value of the output species X_2 at steady state is given by

$$x_{2_{ss}}^{SC} = \frac{\tilde{\mu}}{\tilde{\theta}} \frac{\frac{\alpha_{z_1}}{\gamma_{z_1}}}{\frac{\alpha_{z_2}}{\gamma_{z_2}}} \frac{\rho_{z_1}}{\rho_{z_2}} Y_d. \tag{20}$$

B. Multicellular AIC with Metabolic Burden

We next derive an aggregate model describing the mean dynamics of species concentrations in the multicellular AIC consortium. We use superscripts c and t to denote quantities averaged over Controller and Target populations, respectively. The protein concentration dynamics in the Target population are defined by:

$$\begin{aligned} \dot{x}_1 &= \tilde{\beta}_u \rho_{x_1} \frac{\alpha_{x_1}}{\gamma_{x_1}} R^t q_u^t - \gamma_t x_1, \\ \dot{x}_2 &= \tilde{\beta}_2 \rho_{x_2} \frac{\alpha_{x_2}}{\gamma_{x_2}} R^t x_1 - \gamma_t x_2, \\ \dot{q}_x^t &= \tilde{\beta}_x x_2 + \eta (q_x^e - q_x^t) - \gamma_t q_x^t, \end{aligned} \tag{21}$$

where $\tilde{\beta}_u$ represents the production rate associated to x_1 due to Q_u, $\tilde{\beta}_x$ the production rate of Q_x due to X_2, and R^t represents the average concentration of free resources inside the Targets. Quorum sensing molecules are assumed to be synthesized by means of enzymatic reactions, thus they do not utilize ribosomes.

Similarly, the aggregate dynamics in the Controllers is described by

$$\begin{aligned} \dot{z}_1 &= \tilde{\mu} \rho_{z_1} \frac{\alpha_{z_1}}{\gamma_{z_1}} R^c Y_d - \gamma_z z_1 z_2, \\ \dot{z}_2 &= \tilde{\theta} \rho_{z_2} \frac{\alpha_{z_2}}{\gamma_{z_2}} R^c q_x^c - \gamma_z z_1 z_2, \\ \dot{q}_u^c &= \tilde{\beta}_I z_1 + \eta (q_u^e - q_u^c) - \gamma_c q_u^c, \end{aligned} \tag{22}$$

where R^c represents the average concentrations of free resources in the Controllers.

The expressions of R^c and R^t are different from the one defined in (19). Specifically, within the Controllers only Z_1 and Z_2 take up resources, whereas in the Targets X_1 and X_2 are the only species sharing resources.

The relationship that describes the utilization of resources in the h-th cell of population $j \in \{c,t\}$ can be formalized as

$$R_{T,h}^j = R_h^j + \sum_{i=1}^{n_j} c_{i,h}^j, \tag{23}$$

where $R_{T,h}^j$, R_h^j, and $c_{i,h}^j$ represent the concentration of total resources, of free resources and of translation complexes in population j, respectively, and $n_j = 2$ is the number of chemical species sharing of ribosomes within population j.

Averaging (23) over the entire population j, e.g. c, yields

$$\begin{aligned} \frac{1}{N_c} \sum_{h=1}^{N_c} R_{T,h}^c &= \frac{1}{N_c} \sum_{h=1}^{N_c} R_h^c + \frac{1}{N_c} \sum_{h=1}^{N_c} \sum_{i=1}^{n} c_{i,h}^c \\ \implies R_T^c &= R^c + \sum_{i=1}^{n} \left(\frac{1}{N_c} \sum_{h=1}^{N_c} c_{i,h}^c \right) \end{aligned} \tag{24}$$

where N_c is the number of cells in the Controller population.

Substituting (12) in (24) in place of the average concentration of translation complex c_i^c and solving for R^c, we get

$$R^c = \frac{R_T^c}{1 + \rho_{z_1} \frac{\alpha_{z_1}}{\gamma_{z_1}} Y_d + \rho_{z_2} \frac{\alpha_{z_2}}{\gamma_{z_2}} q_x^c}, \tag{25}$$

where R_T^c and R^c represent the average concentration of total and free resources in the Controller population, respectively.

Following similar steps, we get

$$R^t = \frac{R_T^t}{1 + \rho_{x_1} \frac{\alpha_{x_1}}{\gamma_{x_1}} q_u^t + \rho_{x_2} \frac{\alpha_{x_2}}{\gamma_{x_2}} x_1}, \tag{26}$$

where R_T^t and R^t represent the average concentration of total and free resources in the Target population, respectively.

In order to derive the analytical expression of the output at steady state, we make the following assumptions:

A1. All cells grow and divide at the same rate. This implies that all cells have the same dilution rate: $\gamma_c = \gamma_t = \gamma$. This assumption holds if cells are of the same biological chassis, and thus they grow and divide at the same rate.

A2. The quorum sensing molecules Q_u and Q_x diffuse faster than they degrade. This implies that $\eta \gg \Gamma_I$, with $\Gamma_I := \gamma_c + \gamma_t = 2\gamma$, see e.g. [21].

Under assumptions **A1**-**A2** and provided that there exists a stable, admissible equilibrium point, the value of the output species X_2 at steady state is given by

$$\bar{x}_{2_{ss}} = \frac{\Gamma_I}{\tilde{\beta}_x} \frac{\tilde{\mu}}{\tilde{\theta}} \frac{\frac{\alpha_{z_1}}{\gamma_{z_1}}}{\frac{\alpha_{z_2}}{\gamma_{z_2}}} \frac{\rho_{z_1}}{\rho_{z_2}} Y_d = \frac{\Gamma_I}{\tilde{\beta}_x} x_{2_{ss}}^{SC}. \tag{27}$$

IV. Robustness analysis and in silico experiments

This section compares embedded and multicellular designs based on their ability to regulate X_2 expression to desired levels under resource constraints. We analyze the structural stability of the desired equilibrium point as total resources R_T vary, and validate both architectures through realistic *in silico* agent-based experiments.

To enable direct comparison, we selected parameters Γ_I and $\tilde{\beta}_x$ in the multicellular AIC to match the steady-state values $x_{2_{ss}}^{SC}$ and $\bar{x}_{2_{ss}}$ from equations (20) and (27), respectively.

A. Numerical Bifurcation Analysis

We conducted numerical continuation analysis using MATCONT [22] to identify stable equilibrium ranges for both architectures as total available resources per cell (R_T) vary. For the multicellular AIC, we analyzed equations (21), (22), (8), and (9), assuming equal resources in both populations ($R_T^c = R_T^t = R_T$). The resulting bifurcation diagram (Fig. 2c) shows a saddle-node bifurcation at $R_T = 273.79$ nM (marked as LP, limit point) and a Hopf bifurcation at $R_T = 1544.76$ nM.

The embedded AIC's bifurcation diagram (Fig. 2a) reveals a stable equilibrium point for $R_T \in (679.87;\ 2411.28)$ nM. While this stability range is 36% wider than the multicellular case, the embedded architecture requires three times more minimum resources to operate. Notably, the multicellular AIC achieves stable equilibrium even under scarcer resources per cell, where the embedded design fails to stabilize. Specifically, the multicellular system operates with a total resource level per cell $R_T > 273.79$ nM while the embedded system

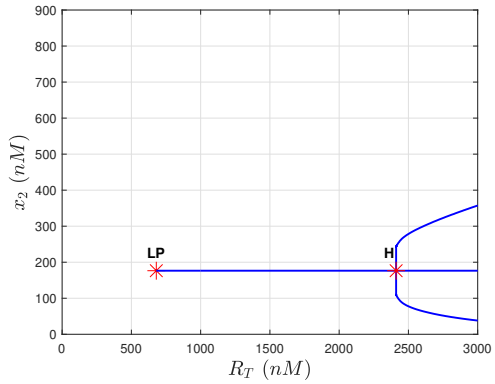

(a) Bifurcation diagram of the equilibrium point of the embedded AIC with burden

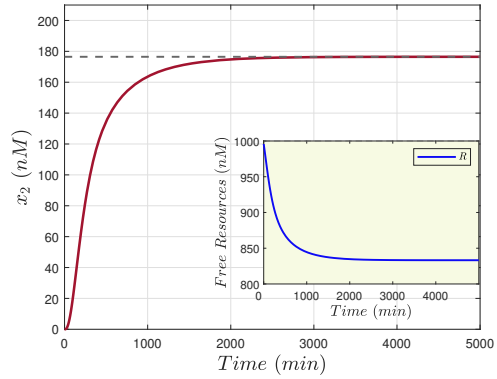

(b) Time evolution of the output and of free resources (inset) in the embedded AIC with burden

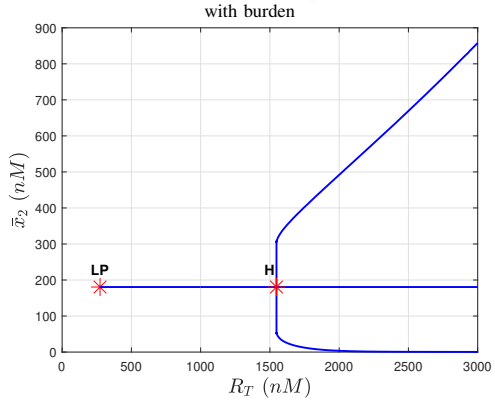

(c) Bifurcation diagram of the equilibrium point of the multicellular AIC with burden

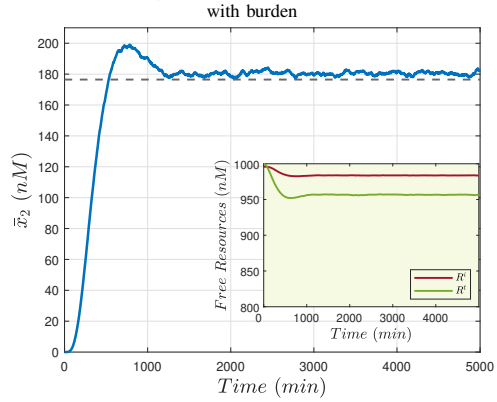

(d) Time evolution of the output and of free resources (inset) in the multicellular AIC with burden

Fig. 2: *In silico* experiments on the embedded and multicellular AIC with burden. Bifurcation diagrams of the equilibrium point of the embedded (a) and multicellular (c) AIC when R_T is chosen as the free parameter. The equilibrium points first undergo a Saddle-Node bifurcation at $R_T = 679.87$ nM and $R_T = 273.79$ nM, respectively, and then a Hopf bifurcation at $R_T = 2411.28$ nM and $R_T = 1544.76$ nM, respectively. Stable equilibrium points exist between the two bifurcations. Time evolution of the output of the embedded (b) and multicellular (d) AIC, respectively. Fluctuations in (d) are due to variation in the number of individuals in each population over time. The introduction of the quorum sensing molecules causes the multicellular steady-state error to be different than zero, in particular $e_{\%} = 2.23\%$. The value of $\tilde{\beta}_I$ was set to 0.066 min^{-1} in the multicellular scenario, and to 0.0857 min^{-1} in the embedded. Insets in Figs. (b) and (d) show time evolution of the free resources in the embedded and multicellular AIC, respectively. In the multicellular scenario, the *controller* population (red line) consumes 1.23% of initial resources, while the *target* population (green line) consumes 4.34%. In the embedded scenario, consumption settles at 16.3% of initial resources. Simulations via *BSim* were carried out in a chamber of dimensions 20 μm $\times$ 15 μm $\times$ 1 μm, starting with 20 bacteria (10 for each population in the multicellular scenario) lined up horizontally in the middle of the chamber. Nominal values of the biochemical parameters are reported in Appendix A.

requires $R_T > 679.87$ nM. Notice that when self-degradation dynamics of Z_1 and Z_2 are also taken into account in the AIC models (21) and (22), a stable equilibrium point still exists for low R_T values. However, the corresponding steady-state value of x_2 goes to zero as R_T decreases, thus the AIC does no more behave as an integral controller.

B. In silico experiments

We validated the multicellular architecture using BSim [15], a realistic agent-based simulator for microbial populations that accounts for physical and geometrical effects including cell-environment interactions, cell growth and replication, and chemical species diffusion in the growth medium. Our simulation chamber (20 $\mu m \times 15$ $\mu m \times 1$ μm) accommodated approximately 75 cells, with top and bottom openings allowing cell turnover through growth and division. Each simulation began with 20 bacteria arranged horizontally in the chamber's middle (split equally between populations in the multicellular scenario).

Figures 2d and 2b demonstrate that both architectures successfully regulate X_2 expression to desired levels, though the multicellular implementation shows some fluctuations due to uneven population turnover. However, from the inset plots in Figures 2d and 2b reporting the time evolution of the free resources in the cells, it is apparent that cells in the embedded architecture consume about three times more resources than those in the multicellular one.

C. Robustness to cell-cell variability

Finally, we tested the robustness of the multicellular architecture's communication mechanism to cell-cell variability. Specifically, we varied the parameters associated with the production and diffusion of the quorum sensing molecules, such as $\tilde{\beta}_I$, $\tilde{\theta}$, $\tilde{\beta}_u$, η, and the concentration of total resources within the cells, that is, R_T. The production rate of Q_x inside the Targets, namely $\tilde{\beta}_x$, was not affected by perturbations, since it is related to the dilution rate of the chemical species in the cells (see Appendix A). Each parameter, say α, was

extracted from a Gaussian distribution centered around the nominal value, $\bar{\alpha}$, with a standard deviation $\sigma = CV \cdot \bar{\alpha}$, where CV represents the coefficient of variation. For each value of $CV \in \{0.05, 0.10, 0.15, 0.20\}$, we performed 10 experiments and evaluated the average steady-state percentage error, defined as

$$\bar{e}_{\%} = \frac{1}{10} \sum_{i=1}^{10} \frac{|\bar{x}_{2,i} - \bar{x}_{2_{ss}}|}{\bar{x}_{2_{ss}}}. \tag{28}$$

where $\bar{x}_{2,i}$ and $\bar{x}_{2_{ss}}$ represent the output concentration averaged over the last 200 minutes in the i-th experiment and the output at steady-state (see equation (27)), respectively. The simulations show that it guarantees small sensitivity to increasing levels of heterogeneity in the communication mechanism and in the total pool of resources, with the average percentage error never exceeding 10%.

V. Conclusions

We developed a resource-aware model for a multicellular implementation of the AIC and compared it with its embedded counterpart. Through numerical continuation analysis and realistic *in silico* experiments, we demonstrated that the multicellular AIC maintains stable equilibrium even under scarce resources (low R_T^c and R_T^t), while the embedded implementation requires substantially higher resource levels per cell for operation. This reduction in resource consumption has important practical implications. Lower metabolic burden translates to faster growth rates and improved culture viability, critical factors for industrial applications. Moreover, the reduced resource requirements suggest that multicellular implementations could better accommodate more complex synthetic circuits, where resource competition often leads to circuit failure.

Future work will focus on deriving analytical conditions for parameter selection to guarantee stable equilibrium points. We also plan to extend this analysis to compare the complete multicellular PID controller [14] with its embedded counterpart [16].

Appendix

A. Nominal Biochemical Parameters

The nominal biochemical parameters used in Matcont numerical continuations and BSim simulations are chosen as: $\tilde{\beta}_2 = 0.148$ min^{-1}, $\tilde{\mu} = 1.428$ min^{-1}, $\tilde{\theta} = 0.486$ min^{-1}, $N_c = N_t = N = 35$, $\rho_{x_1} = \rho_{x_2} = \rho_{z_1} = \rho_{z_2} = 10^{-5}$ nM^{-1}; $\gamma = 0.023$ min^{-1}, $\gamma_e = 0.0023$ min^{-1}, $\tilde{\beta}_u = 0.6$ min^{-1}, $\tilde{\beta}_x = 2\gamma$, $\eta = 2$ min^{-1} (taken from [13]); $Y_d = 60$ nM, $\gamma_z = 0.01$ min^{-1}nM^{-1} (taken from [16]); $R_T = 1000$ nM, $\alpha_X/\gamma_X = 7$, with $X \in \{X_1, X_2, Z_1, Z_2\}$ (taken from [10]).

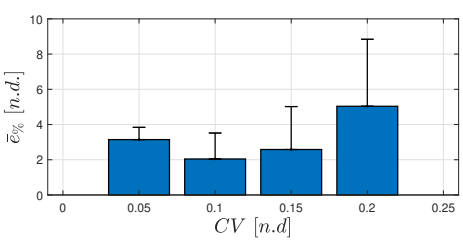

Fig. 3: *In silico* robustness experiments in *BSim*. The multicellular architecture's communication mechanism was tested against cell-to-cell variability. Each parameter, say α, was extracted from a Gaussian distribution centered around the nominal value, $\bar{\alpha}$, and with standard deviation $\sigma = CV \cdot \bar{\alpha}$, where CV represents the coefficient of variation. For each value of $CV \in \{0.05, 0.10, 0.15, 0.20\}$, we evaluated the steady-state percentage error (28) averaged over 10 experiments. The simulations were set up as described in Section IV-B.

References

[1] T. Danino, *et al.*, "Programmable probiotics for detection of cancer in urine," *Science Translational Medicine*, vol. 7, no. 289, pp. 1–28, 2015.

[2] J. C. Anderson, *et al.*, "Environmentally controlled invasion of cancer cells by engineered bacteria," *Journal of Molecular Biology*, vol. 355, no. 4, pp. 619–627, 2006.

[3] D. F. Savage, *et al.*, "Defossiling fuel: How synthetic biology can transform biofuel production," *ACS Chemical Biology*, vol. 3, no. 1, pp. 13–16, 2008.

[4] J. Sinha, *et al.*, "Reprogramming bacteria to seek and destroy an herbicide," *Nature Chemical Biology*, vol. 6, no. 6, pp. 464–470, 2010.

[5] C. Briat, *et al.*, "Antithetic integral feedback ensures robust perfect adaptation in noisy biomolecular networks," *Cell Systems*, vol. 2, no. 1, pp. 15–26, 2016.

[6] S. K. Aoki, *et al.*, "A universal biomolecular integral feedback controller for robust perfect adaptation," *Nature*, vol. 570, no. 7762, pp. 533–537, 2019.

[7] G. Wu, *et al.*, "Metabolic burden: Cornerstones in synthetic biology and metabolic engineering applications," *Trends in Biotechnology*, vol. 34, no. 8, pp. 652–664, 2016.

[8] B. R. Glick, "Metabolic load and heterologous gene expression," *Biotechnology Advances*, vol. 13, no. 2, pp. 247–261, 1995.

[9] K. Sechkar, *et al.*, "A coarse-grained bacterial cell model for resource-aware analysis and design of synthetic gene circuits," *Nature Communications*, vol. 15, no. 1, Mar. 2024.

[10] Y. Qian, *et al.*, "Resource competition shapes the response of genetic circuits," *ACS Synthetic Biology*, vol. 6, no. 7, pp. 1263–1272, 2017.

[11] A. Patel *et al.*, "Exploiting resource constraints for controlling biomolecular circuits," in *Proc. of the 62nd IEEE Conference on Decision and Control*. IEEE, 2023, pp. 2699–2705.

[12] G. Fiore, *et al.*, "In-silico analysis and implementation of a multicellular feedback control strategy in a synthetic bacterial consortium," *ACS Synthetic Biology*, vol. 6, no. 3, pp. 507–517, 2016.

[13] V. Martinelli, *et al.*, "Multicellular PI control for gene regulation in microbial consortia," *IEEE Control Systems Letters*, vol. 6, pp. 3373–3378, 2022.

[14] ——, "Multicellular PID control for robust regulation of biological processes," *Journal of The Royal Society Interface*, vol. 22, no. 222, Jan. 2025.

[15] A. Matyjaszkiewicz, *et al.*, "Bsim 2.0: An advanced agent-based cell simulator," *ACS Synthetic Biology*, vol. 6, no. 10, pp. 1969–1972, 2017.

[16] M. Chevalier, *et al.*, "Design and analysis of a proportional-integral-derivative controller with biological molecules," *Cell Systems*, vol. 9, no. 4, pp. 338–353, 2019.

[17] Y. Chen, *et al.*, "Emergent genetic oscillations in a synthetic microbial consortium," *Science*, vol. 349, no. 6251, pp. 986–989, 2015.

[18] V. Martinelli *et al.*, "Multicellular PD control in microbial consortia," *IEEE Control Systems Letters*, vol. 7, pp. 2641–2646, 2023.

[19] S. Klumpp, *et al.*, "Growth rate-dependent global effects on gene expression in bacteria," *Cell*, vol. 139, no. 7, pp. 1366–1375, 2009.

[20] U. Alon, *An introduction to systems biology: design principles of biological circuits*. Chapman and Hall/CRC, 2006.

[21] D. Fiore, *et al.*, "Multicellular feedback control of a genetic toggle-switch in microbial consortia," *IEEE Control Systems Letters*, vol. 5, no. 1, pp. 151–156, jan 2021.

[22] A. Dhooge, *et al.*, "New features of the software matcont for bifurcation analysis of dynamical systems," *Mathematical and Computer Modelling of Dynamical Systems*, vol. 14, no. 2, pp. 147–175, 2008.